JOURNAL OF GEOPHYSICAL RESEARCH, VOL. 89, NO. B2, PAGES 1089–1104, FEBRUARY 10, 1984

A Detailed View of the South Pacific Geoid From Satellite Altimetry

DAVID T. SANDWELL

National Geodetic Survey, Charting and Geodetic Services, National Ocean Service, NOAA

Images of sea surface undulations in the South Pacific have been constructed from GEOS 3 and SEASAT altimeter data. Height discrepancies at crossover points, associated with long-wavelength radial orbit error, were suppressed by taking along-track derivatives of the ascending and descending profiles. These geoid slopes were then rotated and scaled to produce the north and east components of the deflection of the vertical. Finally, the results are displayed by using the hill shading technique, where gray-tone images represent the innner product of the deflection vector with an assigned sun vector. Less apparent sea surface undulations can be enhanced by varying the sun's zenith and azimuth. Shorter-wavelength sea surface undulations reflect seafloor topography. For instance, fracture zones (FZ's) appear as elongated sharp steps in the sea surface, while seamounts produce circular bumps. Since large areas of the South Pacific are unsurveyed, many previously undetected features appear on the images. Comparisons with bathymetric charts reveal 72 uncharted seamounts having geoid expressions greater than or equal to Easter Island's expression. The dominant features in the images, however, are the large age-offset FZ's such as the Eltanin and Udintsev FZ's. The images reveal that the Eltanin FZ is connected to the Louisville Ridge; combined they produce a continuous geoid signature across most of the South Pacific. This supports the hypothesis of Hayes and Ewing (1968) that the Louisville Ridge is the northwest extension of the Eltanin FZ.

1. INTRODUCTION

Over the past several years, two orbiting radar altimeters, GEOS 3 and SEASAT, have made precise measurements of sea surface undulations over most of the world's oceans [*Stanley*, 1979; *Born et al.*, 1979]. Except for the 1–2 m sea surface undulations associated with geostrophic flow and tides, the geoid and sea surface coincide. As shown in section 4, these altimeter data are extremely accurate and can resolve geoid signals associated with seafloor topography. This accuracy, along with the dense ocean coverage by these two satellites, enables construction of high-resolution geoid maps over most ocean areas. In well-surveyed areas, accurate geoid maps could be used to discriminate among the various modes of isostatic compensation of seafloor topography. They are more useful, however, in remote southern ocean areas since shorter wavelength geoid undulations can be used to map poorly surveyed and uncharted fracture zones (FZ's) [*Sandwell and Schubert*, 1982*a*; *Sailor and Okal*, 1983] as well as to locate and identify previously undetected large seamounts [*Lazarewicz and Schwank*, 1982; *Lambeck and Coleman*, 1982]. Moreover, orientations of fracture zones reflect relative plate motions in the past and, therefore, place constraints on plate reconstruction models [*Menard and Atwater*, 1968]. In addition to these geophysical applications, the maps are useful for geodesy. The two components of the deflection of the vertical, which are equal to the geoid gradient components divided by the earth's radius, are used for point positioning and inertial navigation.

In this study, deflection of the vertical maps of the South Pacific were constructed from GEOS 3 and SEASAT altimeter data. The technique for producing a two-dimensional surface from a network of individual altimeter profiles is designed to (1) enhance geoid undulations associated with FZ's, seamounts, and hot-spot swells; (2) reduce effects of radial ephemeris error; and (3) produce an easily interpreted surface. Because of these special requirements, the map construction technique presented here differs substantially from the crossover minimization techniques used in the past [*Rapp*, 1979; *Marsh et al.*, 1980]. It consists of local mathematical operations such as differentiation and rotation, making it easy to implement. Furthermore, it runs rapidly on a minicomputer and uses less than 30,000 bytes of core memory.

The biggest problem encountered in this study, and in other studies using SEASAT data, is to retain some of the along-track resolution of the individual profiles without introducing artificial undulations caused by poor sampling in the cross-track direction. This problem is alleviated somewhat by incorporating the less accurate GEOS 3 altimeter data in the small gaps between the more accurate SEASAT altimeter profiles.

To justify the map construction technique and to understand the various features of the geoid, it is necessary to review the physical mechanisms that maintain geoid undulations. This is done in the next section (section 2), where a survey is made of the various forms of isostatic compensation of seafloor topography, in particular the thermal compensation mechanism associated with oceanic FZ's and hot-spot swells. The altimetric technique for constructing subsatellite geoid profiles from both altimeter and tracking data is also briefly discussed in section 2. Uncorrected errors in individual geoid profiles, caused by errors in the satellite's radial position, will introduce false short-wavelength "stripes" in geoid maps. Consideration of this ephemeris error along with the topographically produced geoid undulations leads to a simple map construction technique, discussed in section 3. Sampling problems, interpolation schemes, and image processing techniques are discussed in section 3 as well. Finally, gray-tone images of the geoid, constructed from the two components of the deflection of the vertical, are presented in section 4. The images are compared with recent bathymetric charts of the South Pacific to locate a number of previously undetected large seamounts. In addition, the images reveal the detailed structure of the poorly surveyed Eltanin EZ and Louisville Ridge as well as many smaller FZ's.

2. RELATIONSHIP BETWEEN GEOID HEIGHT AND TOPOGRAPHY

Undulations in the shape of the mean sea surface, or geoid, are caused by laterally inhomogeneous mass distribution

Paper number 3B1739.

within the earth. These mass anomalies are physically supported by deviatoric stresses arising either from convective motions of the viscous mantle or from static loads on the rigid lithosphere. Mantle-wide convection maintains many of the longer-wavelength ($>10^6$ m), larger-amplitude (>10 m) geoid undulations [*Kaula*, 1972]. Indeed, a number of studies point out the high correlation between geoid undulations and the surface manifestations of mantle convection, such as spreading ridges, subduction zones, and hot-spot swells [*Haxby and Turcotte*, 1978; *Sandwell and Schubert*, 1980; *Griggs*, 1972; *Crough and Jurdy*, 1980].

While the geoid is dominated by these longer-wavelength undulations, much of the information is contained in the shorter-wavelength ($<10^6$ m) undulations. These signals primarily originate from density anomalies within the lithosphere. In all but a few extreme cases, shorter-wavelength geoid undulations are highly correlated with seafloor topography. This correlation has been used in well-surveyed areas to estimate the thermal and mechanical properties of the oceanic lithosphere. In poorly surveyed areas, however, topography could be estimated from geoid undulations if the isostatic compensation mechanism was known. Unfortunately, the relationship between geoid height and topography is nonunique because of the different topographic compensation mechanisms.

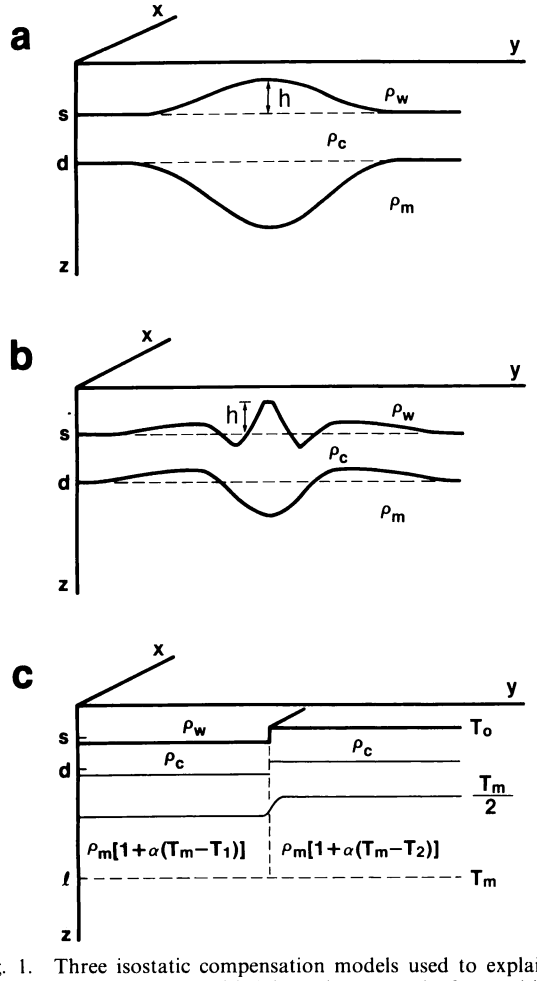

Fig. 1. Three isostatic compensation models used to explain the correspondence between geoid height and topography h. Densities ρ_w, ρ_c, and ρ_m are the water, crustal, and mantle densities, respectively. (*a*) The Airy compensation model has an average compensation depth d of 11 km, resulting in a relatively low geoid/topography ratio. (*b*) The geoid/topography ratio for the regional compensation model depends strongly upon the strength of the lithosphere (see Figure 2). (*c*) Topography across a fracture zone is supported by thermal buoyancy forces caused by lateral temperature variations T_1 and T_2. This relatively deep compensation results in a high geoid/topography ratio.

A number of isostatic compensation mechanisms have been proposed to account for the various types of seafloor morphology. For each mechanism, the relationship between geoid height and topography is nearly linear and primarily depends upon the wavelength of the topography. The smallest geoid undulations or gravity anomalies occur over topography that is locally compensated at the crust-mantle boundary. The Airy local compensation model, shown in Figure 1*a*, can explain both the high crustal thickness and the low gravity/topography ratios over oceanic plateaus [*Den et al.*, 1969; *Hussong et al.*, 1979], portions of aseismic ridges [*Kogan*, 1976; *Detrick and Watts*, 1979], and seamounts formed near ocean ridges [*McNutt*, 1979]. In this model the depth to the Moho is adjusted to maintain a constant mass in every vertical column.

The relationship between geoid height and topography is most easily expressed in the Fourier transform domain [*Dorman and Lewis*, 1970]

$$\frac{N(\mathbf{k})}{H(\mathbf{k})} = \frac{2\pi G(\rho_c - \rho_w)}{g|\mathbf{k}|} e^{-|\mathbf{k}|s}(1 - e^{-|\mathbf{k}|d}) \tag{1}$$

where $\mathbf{k}$ is the wave number (i.e., 2π/wavelength), and $N(\mathbf{k})$ and $H(\mathbf{k})$ are the Fourier transforms of the geoid height and topography h, respectively. The transfer function on the right side of (1) contains model parameters (ρ_w is water density of 1025 kg m^{-3}, ρ_c is crustal density of 2800 kg m^{-3}, s is water depth of 5 km, and d is Moho depth of 11 km) as well as G, the universal gravitational constant, and g, the gravitational acceleration. It depends only upon the magnitude of the wave number through the two exponential upward continuation factors. This Airy transfer function, shown in Figure 2 (solid curve), has relatively low amplitude ($\sim$.4 m/km) over the whole wavelength band and begins to decrease exponentially at a wavelength of 2π times the water depth ($\sim$30 km) because of upward continuation through the water column. Based upon these calculations, seafloor topography that is nearly Airy-compensated will not appear strongly on geoid height maps.

Topography that formed on mature lithosphere, i.e., lithosphere that has had time to cool and strengthen, is not compensated by a local increase in crustal thickness. Instead, the lithosphere flexes to distribute the load over a broader area (i.e., regional compensation), as shown in Figure 1*b*. The flexure model, which incorporates a thin elastic plate (lithosphere) overlaying a fluid half space (asthenosphere), has been used for quantitative modeling of regional compensation [*Turcotte*, 1974]. The geoid/topography relationship for this model can also be expressed as a linear transfer function [*McKenzie and Bowin*, 1976; *Banks et al.*, 1977]

$$\frac{N(\mathbf{k})}{H(\mathbf{k})} = \frac{2\pi G(\rho_c - \rho_w)}{g|\mathbf{k}|} e^{-|\mathbf{k}|s}\left\{1 - \left[1 + \frac{D|\mathbf{k}|^4}{g(\rho_m - \rho_c)}\right]^{-1} e^{-|\mathbf{k}|d}\right\} \tag{2}$$

where ρ_m is the mantle density of 3300 km m^{-3}. The flexural rigidity D characterizes the strength of the lithosphere, and it is proportional to the cube of the thickness of the elastic plate.

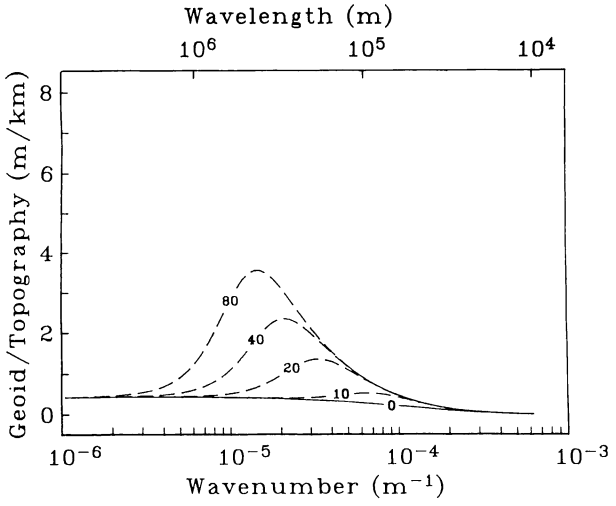

Fig. 2. Geoid/topography transfer function for Airy compensation model (solid curve) and regional compensation models (dashed curves). Numbers along each curve indicate the age of the lithosphere, in millions of years, at the time the topography formed. The large changes with age occur because the elastic part of the lithosphere thickens as the lithosphere cools.

This model explains the relatively high gravity/topography ratios associated with seamounts along the Hawaiian Chain [*Gunn*, 1943; *Walcott*, 1970] as well as seamounts in the Western Pacific [*Watts and Ribe*, 1984]. *Watts* [1978] examined the gravity/topography transfer functions for a number of seamounts along the Hawaiian-Emperor Chain and determined that the flexural rigidity is largely dependent upon the age of the lithosphere when the seamount formed. Young lithosphere has low rigidity and flexes readily under the load of a seamount, whereas a seamount emplaced upon older, stronger lithosphere has a broad low-amplitude flexure profile. This strength-age relationship also explains the differences in the wavelength and amplitude of outer rise topography at subduction zones [*Caldwell and Turcotte*, 1979]. As shown in Figure 2, these differences in lithosphere strength have a large effect upon the geoid height. The dashed curves in Figure 2 are geoid/topography transfer functions for topography formed on lithosphere with ages of 0, 10, 20, 40, and 80 m.y. (i.e., using Caldwell and Turcotte's relationship between flexural rigidity and age). As the lithosphere ages, the amplitude of the geoid topography transfer function increases and the peak value shifts to longer wavelengths. This large range in the geoid/topography transfer function explains why two seamounts that formed at different times, but are otherwise identical, have vastly different geoid signatures. The geoid images presented in section 4 substantiate this strength-age relationship, since the amplitudes of geoid undulations produced by seamounts formed on the young lithosphere near the East Pacific Rise are generally small or absent. On older lithosphere, however, geoid undulations over seamounts can be more prominent.

Relatively large, short-wavelength ($<10^6$ m) geoid undulations also occur over topography that is thermally compensated [*Haxby and Turcotte*, 1978]. Features such as spreading ridges, fracture zones, and hot-spot swells are nearly in local isostatic equilibrium and are physically supported by thermal buoyancy forces arising from lateral variations in lithosphere temperature. Figure 1*c* shows a simplified view of the temperature, density, and topography across an FZ. The lithosphere on the left side of the FZ is older, cooler, and more dense than the lithosphere on the right side. It is in isostatic equilibrium because the water depth on the left side is greater than the depth on the right side. This simple model does not include the effects of thermomechanical coupling across the FZ, which were found to be important when modeling FZ topography [*Sandwell and Schubert*, 1982*b*]. Nevertheless, it reproduces the gravity field and geoid heights across FZ's [*Sibuet and Mascle*, 1978; *Crough*, 1979; *Detrick*, 1981; *Sandwell and Schubert*, 1982*a*; *Cazenave*, 1982]. Across the younger portions of FZ's (<40 m.y.), the geoid height increases in a steplike fashion from the older lithosphere to the younger lithosphere. For example, the geoid step across large age offset FZ's (20–30 m.y.) is 3 to 4.5 m. The step amplitude, however, decreases substantially as the age of the FZ exceeds 40 m.y.

The geoid/topography transfer function for this FZ model is shown in Figure 3 (solid curve). The analytic expression for the thermal compensation transfer function is the ratio of equations (B4) and (B5) in *Sandwell* [1982] and was calculated by using a thermal expansion coefficient of 3.1×10^{-5} K^{-1}, a heat capacity of 1172 J kg^{-1} K^{-1}, a thermal diffusivity of 8.0×10^{-7} m^2 s^{-1}, an asymptotic lithospheric thickness of 128 km, a mantle temperature of 1638 K, a seafloor temperature of 273 K, and a flexural rigidity of zero. The amplitude of this tranfer function is greater than the transfer function for regionally compensated topography that formed on 80 m.y. old lithosphere (Figure 2).

The final type of seafloor morphology considered here is the hot-spot swell. These broad elongated swells in the seafloor are produced as mature lithosphere passes over the upwelling limb of a convective plume [*Wilson*, 1963]. Much of the seafloor swell and corresponding geoid high can be attributed to local increases in the lithospheric temperatures [*Detrick and Crough*, 1978; *Crough*, 1978; *Sandwell and Poehls*, 1980]. The geoid/topography transfer function corresponding to a hot-spot swell is shown in Figure 3 (dashed curve). For this model the lithosphere was thinned from 128 km to 40 km, and it has the flexural rigidity of 40 m.y. old lithosphere. Because of this high rigidity, the transfer function drops rapidly near the flex-

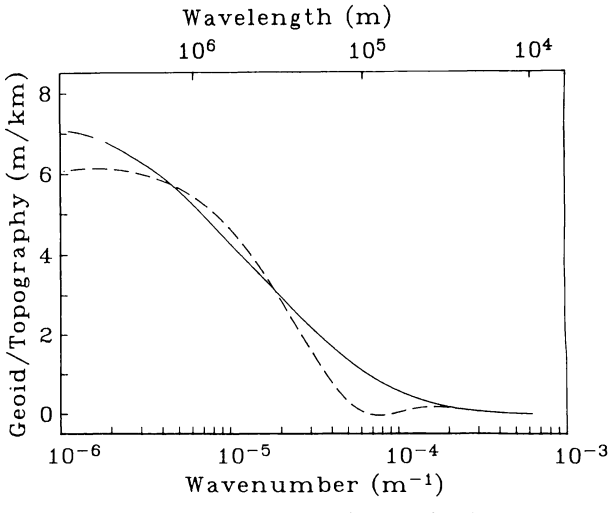

Fig. 3. Geoid/topography transfer function for the thermal compensation model. Solid curve applies to an oceanic FZ. The hot-spot swell transfer function (dashed curve) is relatively low at 100 km because of lithospheric strength.

ural wavelength ($\sim$300 km). At longer wavelengths, however, the transfer function is relatively large (6 m/km) because most of the compensation occurs at depths greater than 40 km.

This discussion of the theoretical and observational relationship between geoid height and topography not only helps when interpeting the geoid images (section 4) but provides a theoretical foundation for designing filters to enhance the topographic geoid signal. Assuming a "white" topography power spectrum, the transfer functions (Figures 2 and 3) show that most of the topographic geoid signals will be composed of wavelengths greater than 30 km. As stated previously, the mantle convection geoid signal dominates the longer-wavelength geoid undulations ($>10^6$ m). Thus the optimal filter for enhancing the topographic geoid signal should suppress the longer-wavelength geoid undulations; it should also suppress the errors in the measurements. In addition, the filter must be smooth in both the space domain and the wave number domain to avoid artificial undulations [*Bracewell*, 1978]. This is especially true when high-pass filtering a function with a "red" spectrum, such as the earth's geoid.

Altimeter and Ephemeris Error

Errors associated with altimetric sea surface height measurements fall into three categories: those that can be modeled or edited from the data, the altimeter noise, and the radial epheremis error. Each error type is handled differently.

Errors or path effects that have been successfully modeled arise from variations in microwave velocity, from solid earth and ocean tides, from atmospheric pressure variations, and from ocean waves. The SEASAT data were corrected for the important effects by using correction factors described in the Geophysical Data Record Users Handbook [*Lorell et al.*, 1980]. The GEOS 3 data were also corrected, although the water vapor correction was modeled [*Stanley and Dwyer*, 1980]. The SEASAT data were edited using the following criteria: land data, tilt angle out of limits, height blunder, significant wave height blunder, automatic gain control outside the range 32–60 db, and rms of height frame average >0.5 m. GEOS 3 data editing criteria were similar: global model data, auto track, APG/AASG edit, Kalman edit, and automatic gain control outside the range 67–79 db. Other obvious blunders, such as latitudes exceeding 90°, were also edited. Most of the bad SEASAT data were acquired near the Antarctic ice sheet [*Marsh and Martin*, 1982], while bad GEOS 3 data points are randomly distributed geographically. Outlying points were effectively removed by this editing procedure.

Unmodeled altimeter error, or noise, generally has low amplitude and consists mainly of short wavelength (<60 km). *Brammer and Sailor* [1980] investigated the noise spectrum for SEASAT data and found that very short wavelength noise (13–33 km) has amplitudes of $\sim$50 mm. Through analysis of colinear passes they also found a high coherence between passes for wavelengths greater than 60 km. A similar analysis [*Brammer*, 1979], using GEOS 3 data, demonstrates that for wavelengths greater than 60 km the geoid signal exceeds the altimeter noise. Since the signals of interest in this study have amplitudes exceeding 0.5 m and wavelengths greater than 30 km the altimeter noise is not a major problem.

The largest errors occur because of mislocating the satellite with respect to the reference ellipsoid. Estimates of the radial ephemeris error, based upon height discrepancies of crossover points, are 1 to 2 m rms for SEASAT data [*Marsh and Williamson*, 1980] and 1.8 m rms for the first 1.5 years of GEOS 3 data [*Lerch et al.*, 1978]. The radial orbit error for the remaining 2.5 years of GEOS 3 data is slightly higher (S. Klosko, personal communication, 1983). Fortunately, this radial ephemeris error has a dominant period of once per revolution. Removal of biases and trends from passes a few thousand kilometers in length eliminates most of the orbit error. Typical bias and slope errors for GEOS 3 orbit errors are 1.5 m and 0.15 μrad, respectively (1 arc sec = 4.848 μrad = 0.5630 m/deg) [*Douglas et al.*, 1983]. Extreme slopes in GEOS 3 orbit error are 0.4 μrad. For periods of less than one third of a revolution the amplitude of the SEASAT orbit error is less than 50 mm, corresponding to a slope error of about 0.02 μrad [*Marsh and Williamson*, 1980]. As shown in section 4, typical values for the deflections of the vertical associated with seafloor topography are 15 μrad. These angles are about 100 times the slope errors in the GEOS 3 orbit and 750 times the SEASAT slope errors. Thus when geoid slopes rather than the geoid heights are used the orbit error is suppressed far below the typical topographic geoid signals.

3. Gradient Estimation, Interpolation, and Image Processing

Differentiation of each altimeter profile not only suppresses radial ephemeris error but also acts as a high-pass filter. After differentiation, short-wavelength geoid undulations have about the same amplitudes as the long wavelength undulations. A network of differentiated profiles can be used to construct deflection of the vertical maps and sun illumination images. Consider for the moment the subsatellite tracks of a single satellite, as shown in Figure 4*a*. The derivative of the geoid height, with respect to time, along the ascending pass is

$$\frac{\partial N_1}{\partial t} = \frac{\partial N}{\partial \theta}\frac{\partial \theta_1}{\partial t} + \frac{\partial N}{\partial \phi}\frac{\partial \phi_1}{\partial t} \tag{3}$$

and along the descending pass is

$$\frac{\partial N_2}{\partial t} = \frac{\partial N}{\partial \theta}\frac{\partial \theta_2}{\partial t} + \frac{\partial N}{\partial \phi}\frac{\partial \phi_2}{\partial t} \tag{4}$$

where N is the geoid height, θ is latitude, ϕ is longitude, and t is time. The subscripts 1 and 2 refer to ascending and descending orbits, respectively. The functions $\partial\theta/\partial t$ and $\partial\phi/\partial t$ are the two components of the satellite's velocity. At a crossover they satisfy the following relations to an accuracy of better than 1%:

$$\frac{\gtrsim \partial\theta_1}{\partial t} = -\frac{\partial\theta_2}{\partial t} \qquad \frac{\partial\phi_1}{\partial t} = \frac{\partial\phi_2}{\partial t} \tag{5}$$

The geoid gradient vector is obtained by solving (3) and (4), using (5)

$$\frac{\partial N}{\partial \theta} = \frac{1}{2|\dot{\theta}|}(\dot{N}_1 - \dot{N}_2) \tag{6}$$

$$\frac{\partial N}{\partial \phi} = \frac{1}{2\dot{\phi}}(\dot{N}_1 + \dot{N}_2) \tag{7}$$

where the dot denotes $\partial/\partial t$. Notice that for near-polar orbits, $\dot{\phi}$ is small and $N_1 \cong -N_2$. In this case the north component of the geoid gradient is well determined, while the east component is poorly determined. The opposite effect occurs at the extreme latitude points of satellites in nonpolar orbits; extreme latitudes for SEASAT are +72° and −72°. The north (ξ) and east (η) components of the deflection of the vertical are

obtainable from the geoid gradient and are

$$\xi = -\frac{1}{a}\frac{\partial N}{\partial \theta} \tag{8}$$

$$\eta = -\frac{1}{a \cos \theta}\frac{\partial N}{\partial \phi} \tag{9}$$

where a is the radius of the earth and the small angle approximation to the tangent function was used (i.e., $\tan(\alpha) \cong \alpha$).

When two or more satellites with different orbital inclinations are incorporated into the above analysis, the situation is slightly more complex. Consider the intersection of four passes from two satellites as shown in Figure 4*b*. To distinguish the passes, they are labeled 1, 2, 3, and 4. The along-track derivative of each pass can be computed from the geoid gradient at the crossover point

$$\begin{bmatrix} \dot{N}_1 \\ \dot{N}_2 \\ \dot{N}_3 \\ \dot{N}_4 \end{bmatrix} = \begin{bmatrix} \dot{\theta}_1 & \dot{\phi}_1 \\ \dot{\theta}_2 & \dot{\phi}_2 \\ \dot{\theta}_3 & \dot{\phi}_3 \\ \dot{\theta}_4 & \dot{\phi}_4 \end{bmatrix} \begin{bmatrix} \frac{\partial N}{\partial \theta} \\ \frac{\partial N}{\partial \phi} \end{bmatrix} \tag{10}$$

Using matrix notation, (10) becomes

$$\dot{\mathbf{N}} = \mathbf{\Theta}\, \nabla N \tag{11}$$

where

$$\nabla \equiv \boldsymbol{\theta}\frac{\partial}{\partial \theta} + \boldsymbol{\phi}\frac{\partial}{\partial \phi}$$

In this case, the inverse problem of solving for the geoid gradient is overdetermined. However, since the derivative of each profile contains some noise with standard deviation $\dot{\sigma}_i$, the best estimate of the geoid gradient will be one that minimizes the weighted distance between the observations N_i and the model M_i

$$\min \sum_{i=1}^{4} \left(\frac{\dot{N}_i - \dot{M}_i}{\dot{\sigma}_i} \right)^2 \tag{12}$$

The values of the weights $\dot{\sigma}_i$ are difficult to estimate, since they represent the standard deviation of the derivative of the noise. However, when two or more data sets have different noise levels the relative values of standard deviations are useful for deemphasizing the noisier data. To solve (12), let

$$\dot{N}_i' = \frac{\dot{N}_i}{\dot{\sigma}_i} \qquad \dot{\theta}_i' = \frac{\dot{\theta}_i}{\dot{\sigma}_i} \qquad \dot{\phi}_i' = \frac{\dot{\phi}_i}{\dot{\sigma}_i} \tag{13}$$

The solution is [*Hamilton*, 1964]

$$\nabla N = (\mathbf{\Theta}'^t \mathbf{\Theta}')^{-1} \mathbf{\Theta}'^t \dot{\mathbf{N}}' \tag{14}$$

where t and -1 are the transpose and inverse operations, respectively. A two by two matrix must be inverted at every crossover point. This technique is easily extended to three or more satellites with different noise levels. However, it can be rigorously applied only at the crossover point of two nonparallel passes.

In addition to the geoid gradient, the covariances are also obtained

$$\mathbf{\Sigma} = (\mathbf{\Theta}'^t \mathbf{\Theta}')^{-1} \tag{15}$$

where

$$\mathbf{\Sigma} = \begin{bmatrix} \sigma_{\theta\theta}{}^2 & \sigma_{\theta\phi}{}^2 \\ \sigma_{\theta\phi}{}^2 & \sigma_{\phi\phi}{}^2 \end{bmatrix} \tag{16}$$

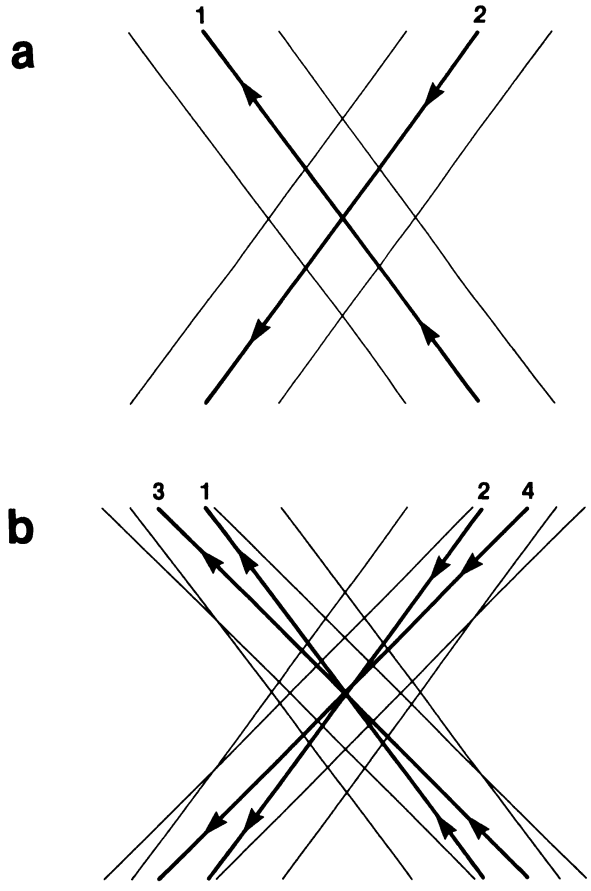

Fig. 4. (*a*) Schematic diagram of SEASAT ground tracks (1, ascending pass; 2, descending pass). (*b*) SEASAT (1 and 2) and GEOS 3 (3 and 4) ground tracks. GEOS 3 data fills some SEASAT data gaps and increases the number of crossover points.

The elements of the covariance matrix depend only upon the quality of the data and the geometry of the passes.

Interpolation

When using both GEOS 3 and SEASAT data the spacings between crossover points varies considerably over the oceans. The largest spacings of up to 80 km occur near the equator in regions of sparse GEOS 3 coverage. Near latitudes of $\pm 72°$ and $\pm 65°$ the crossover spacings are small: 10–20 km. In theory, the shortest wavelength resolvable is equal to twice the sampling interval, so in poorly sampled regions the resolution would be low (~ 160 km), whereas at higher latitudes shorter wavelengths could be resolved. A two-dimensional surface constructed via this conservative approach, however, does not utilize the full along-track resolution of the individual passes. A higher-resolution surface can be constructed by using a priori knowledge of the typical geoid signals produced by the various types of seafloor topography. For example, the geoid gradient surrounding an isolated Airy-compensated seamount decreases approximately as r^{-3}, where r is the distance from the seamount. A variation of this simple model for the autocorrelation function is used in section 4 to interpolate among passes.

Consider the sampling function

$$g_i(\theta, \phi) = \begin{cases} 1 & \text{data exist} \\ 0 & \text{no data} \end{cases} \tag{17}$$

for the ith set of parallel passes. The noise in the geoid gradient along a single pass can be reduced by convolving it with a low-pass filter $\rho(\theta, \phi)$:

$$\dot{N}_i(\theta, \phi) = \frac{\int_0^{2\pi} \int_{-\pi/2}^{\pi/2} \dot{N}_i(\theta_0, \phi_0) g_i(\theta_0, \phi_0) \rho(\theta - \theta_0, \phi - \phi_0)\, d\theta_0\, d\phi_0}{\int_0^{2\pi} \int_{-\pi/2}^{\pi/2} g_i(\theta_0, \phi_0) \rho(\theta - \theta_0, \phi - \phi_0)\, d\theta_0\, d\phi_0} \tag{18}$$

Equation (18) is more concisely written,

$$\overline{\dot{N}}_i = \langle \dot{N}_i g_i, \rho \rangle / \langle g_i, \rho \rangle \tag{19}$$

where $\langle\ ,\ \rangle$ represents the convolution integral. The smooth version of the along-track geoid gradient at θ, ϕ is a weighted average of the the surrounding data points. The sampling function $g_i(\theta_0, \phi_0)$ ensures that areas containing no data are not used. In addition to smoothing along profiles, (18) can be used for interpolating between profiles, since it can be evaluated at points where no data exist. The denominator of (18) or (19) provides a measure of how close the interpolated point is to existing data. For points lying on or near an altimeter pass, $\langle g_i, \rho \rangle$ will have a large value, and the geoid gradient estimate will be accurate. On the other hand, $\langle g_i, \rho \rangle$ will be small for interpolated points far from any data.

The half width of the weight function ρ controls resolution in the map. To retain short-wavelength information, ρ should be narrow. However, artificial undulations will develop in interpolated areas if ρ is much narrower than the track spacing. The optimal width can only be deduced by trial and error.

The weight function is not necessarily isotropic. Its shape also controls the accuracy of the interpolation. For instance, a long but narrow geoid undulation may appear on several parallel passes. A person interpreting these passes would naturally identify the trend and interpolate along it. The interpolation scheme described by (18) could also interpolate properly if the weight function was wide along the strike of the feature and narrow in the perpendicular direction. W. F. Haxby (personal communication, 1983) uses an anisotropic interpolation technique that can determine when trends exist. Unfortunately, this method is incompatible with the crossover technique described above. Other anisotropic interpolation techniques are being tested.

The weight function adopted here is

$$\rho(r) = \frac{1}{1 + (r/\alpha)^3} \tag{20}$$

where

$$r = a(\theta^2 + (\phi \cos \theta)^2)^{1/2} \tag{21}$$

and

$$\alpha = \alpha_0 \cos \theta \qquad \alpha_0 = 30 \text{ km} \tag{22}$$

The parameter α controls the width of the weight function. A plot of ρ versus r/α appears in Figure 5 (solid curve). For comparison purposes the Gaussian function $\exp(r^2/2\alpha^2)$ is also plotted (dashed curve). The two functions are similar, except at large values of r/α, where their slopes are much different.

After convolving the data with the weight function the exact position of the altimeter profile is less important. Indeed, one could image that profiles exist everywhere, although some are more reliable than others. The convolution of the sampling function g_i with the weight function ρ is one measure of reliability, since $\langle g_i, \rho \rangle$ is inversely related to the distance from real data. A smoothed version of the geoid gradient $\overline{\nabla N}$ can now be calculated everywhere by using the two or more sets of interpolated passes. The forward relationship is

$$\frac{\langle \dot{N}_i' g_i, \rho \rangle}{\langle g_i, \rho \rangle} = \dot{\theta}_i' \frac{\overline{\partial N}}{\partial \theta} + \dot{\phi}_i' \frac{\overline{\partial N}}{\partial \phi} \tag{23}$$

Equation (23) is taken as the definition of the smooth geoid gradient. When data from only one satellite are used, the smooth geoid gradient can be estimated through (6) and (7), where N_i is replaced by $\bar{N}_i$. When using data from two or more satellites, however, each data type should be weighted according to its distance from an actual pass of data. This is accomplished by multiplying (23) by the factor $\langle g_i, \rho \rangle$

$$\langle \dot{N}_i' g_i, \rho \rangle = \langle g_i, \rho \rangle \dot{\theta}_i' \frac{\overline{\partial N}}{\partial \theta} + \langle g_i, \rho \rangle \dot{\phi}_i' \frac{\overline{\partial N}}{\partial \phi} \tag{24}$$

This set of equations is solved via the least squares approach described above. The solution is

$$\overline{\nabla N} = (\bar{\Theta}'' \bar{\Theta}')^{-1} \bar{\Theta}'' \bar{\mathbf{N}}' \tag{25}$$

In practice, the convolution integral (18) does not have to extend over the entire surface of the earth. Adequate numerical accuracy is achieved by integrating over a radius of 6α, which corresponds to 200 km (i.e., when using (20)). These convolution integrals involve many computer operations, although they are well suited for parallel processing techniques.

Image Processing

Contour maps of the north and east components of the deflection of the vertical are difficult to interpret, especially for the untrained eye. Perhaps the simplest method for displaying these data is the hill shading technique; it also provides immediate visual impact [*Horn*, 1982]. Consider the sun shining on an irregular surface (e.g., beach sand or snow). An observer sees hills and valleys on the surface by looking at the patterns of brightness. For a small surface element the observed light intensity depends upon the following factors: (1) the direction of the vector between the element and the sun (sun vector), (2) the unit vector between the element and the observer, (3) the unit vector normal to the surface element (e.g., the deflection of the vertical), and (4) the reflectance properties of the surface. Unlike sand and snow, the geoid undulations are much too small to be seen. However, an enhanced geoid image can be created by exaggerating the amplitudes and choosing a reflectance model.

For simplicity the Lambertian reflectance model was adopted. In this model the reflectance is independent of the direction between the surface element and the observer. It depends only upon the cosine of the angle between the sun vector and the unit normal to the geoid. The sun vector $\mathbf{s}$ is specified by an azimuth angle λ, measured counterclockwise from east, and a zenith angle ϕ, measured from vertical, and is

$$\mathbf{s} = (\cos \phi \sin \lambda, \sin \phi \sin \lambda, \cos \lambda) \tag{26}$$

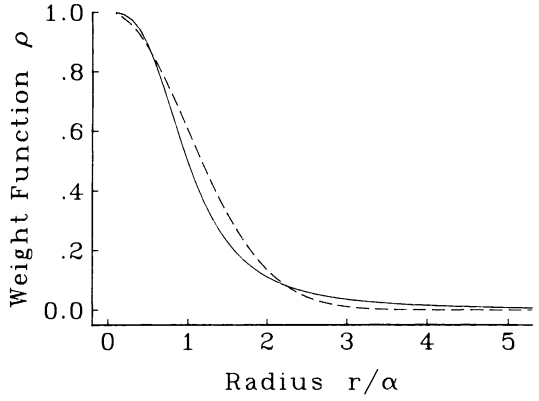

Fig. 5. Weight function (solid curve) that is convolved with the data to both smooth along a pass and interpolate among passes. The Gaussian function (dashed curve) is not suitable for interpolation because it decreases too rapidly when $r/\alpha > 3$, about 80 km.

The normal to the geoid is

$$\mathbf{n} = (\eta, \xi, 1)/(\eta^2 + \xi^2 + 1)^{1/2} \tag{27}$$

where η and ξ are the east and north deflections of the vertical given in (8) and (9). For the marine geoid these deflection angles are extremely small (~ 15 μrad), and under normal lighting conditions, reflectance variations are too small to be seen. If the sun is placed very close to the local horizon, however, (i.e., $\lambda \cong 90°$) the irregularities in the sea surface are amplified. The reflectance R is the dot product of the **s** and **n** vectors

$$R(\mathbf{s}, \mathbf{n}) = \mathbf{s} \cdot \mathbf{n}/|\mathbf{s}|\,|\mathbf{n}| \tag{28}$$

This imaging technique is used in the following section to display deflection of the vertical over the South Pacific.

4. Data Analysis and Results

The area investigated in this study encompasses most of the South Pacific. This area was chosen for two reasons. First, it contains the Eltanin FZ system, which is the largest in the world's oceans. Both theoretical and observational [*Cazenave et al.*, 1983] studies indicate that this FZ dominates the shorter-wavelength geoid undulations in the South Pacific. Second, most of the study area is poorly surveyed. Indeed, there are many regions, some as large as 5° by 5°, that do not contain available depth soundings. Because of this poor sampling, one would expect that many seamounts have not been detected.

A bathymetric chart [*Mammerickx et al.*, 1974] of this

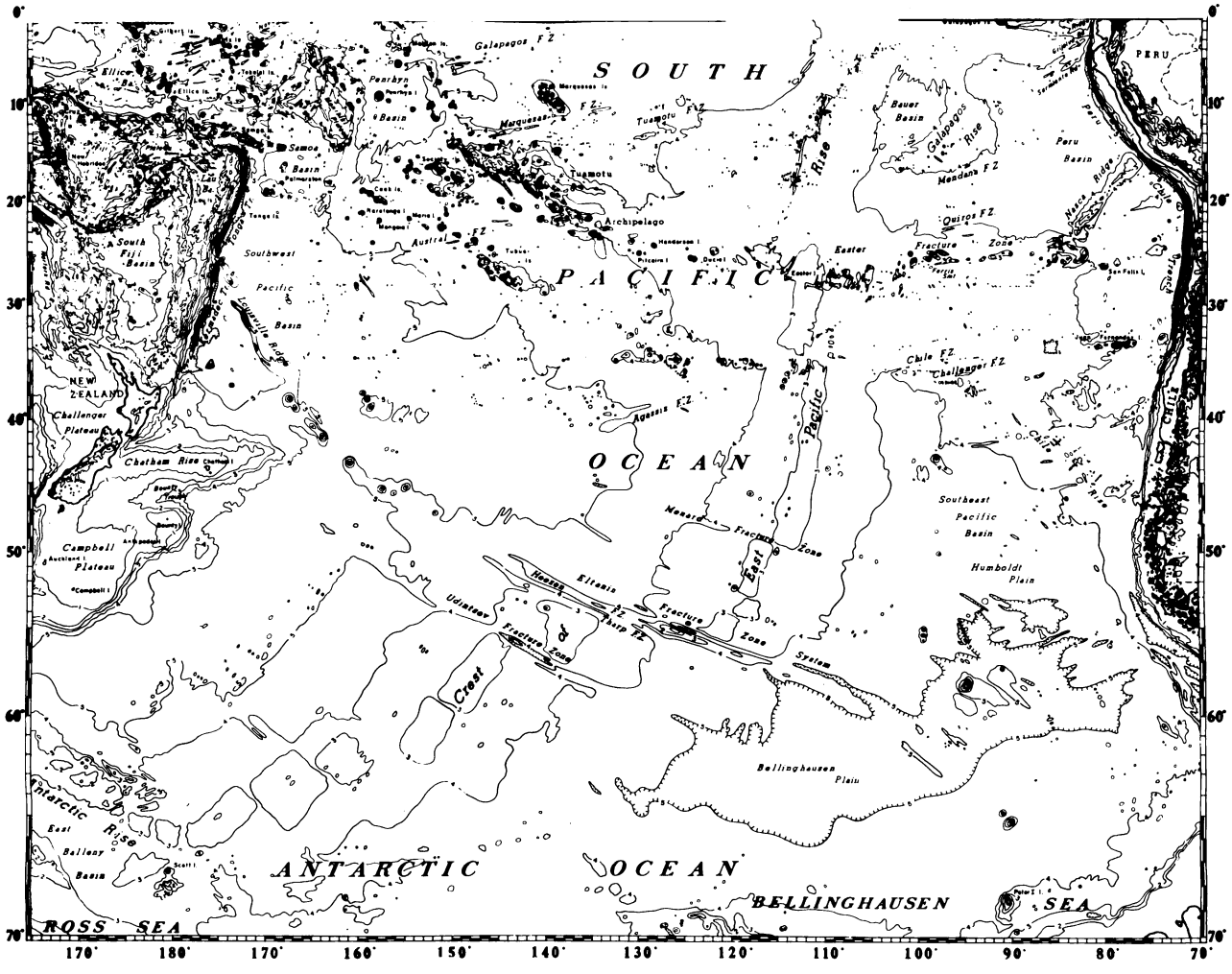

Fig. 6. Bathymetric chart of the South Pacific [after *Mammerickx et al.*, 1974]. Major age offsets in the seafloor occur along the Heezen, Tharp and Udintsev FZ's. Bathymetric coverage of this area is sparse.

region is shown in Figure 6. The major features are the East Pacific Rise, which is offset by about 700 km at the Eltanin FZ system; the Chile Rise; the Kermadec and Tonga trenches, which are bisected by the Louisville Ridge; and the Sala y Gomez Ridge and the Nasca Ridge. In addition, the area contains many seamounts and smaller FZ's. Compared with other ocean areas, the bathymetry of the South Pacific appears smooth. This is largely due to an absence of bathymetry data.

In contrast to the poor bathymetric coverage of this area, the coverage by the SEASAT and GEOS 3 altimeters is dense and relatively uniform. The ground tracks of edited SEASAT and GEOS 3 data are shown in Figures 7*a* and 7*b*, respectively. Each track represents a sequence of closely spaced ($\sim$7 km) data points, and each data point is an average of 1000 radar pulses. Before editing, there are 6.0×10^5 SEASAT data points and 2.9×10^5 GEOS 3 data points. Much of the SEASAT data below $-65°$ were edited because of sea ice. Editing of GEOS 3 data also removed a large number of points.

Except in the sea ice area, the SEASAT data distribution is uniform. The largest data gaps are diamond shaped and have dimensions of about 100 km. The GEOS 3 data distribution is

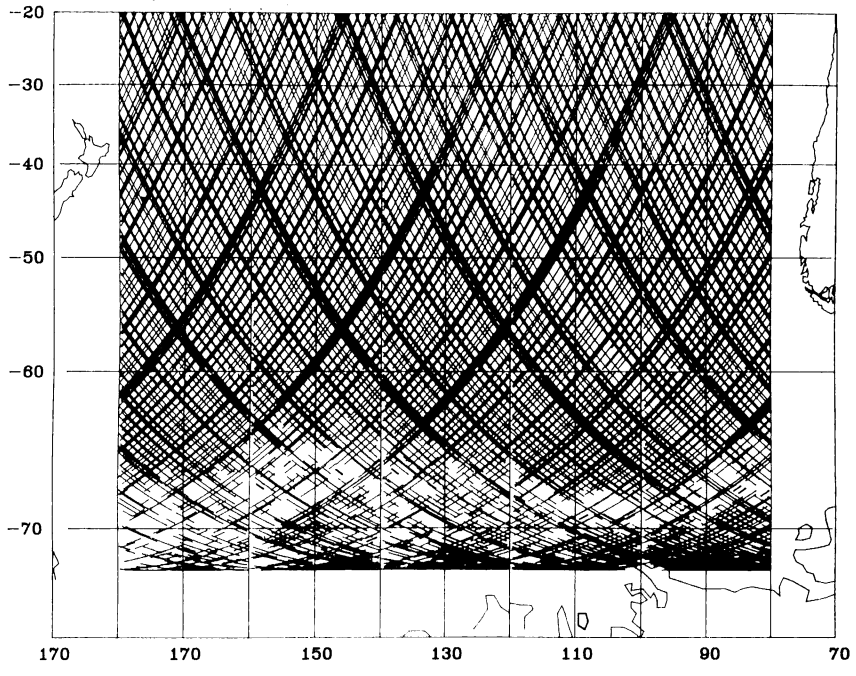

Fig. 7*a*

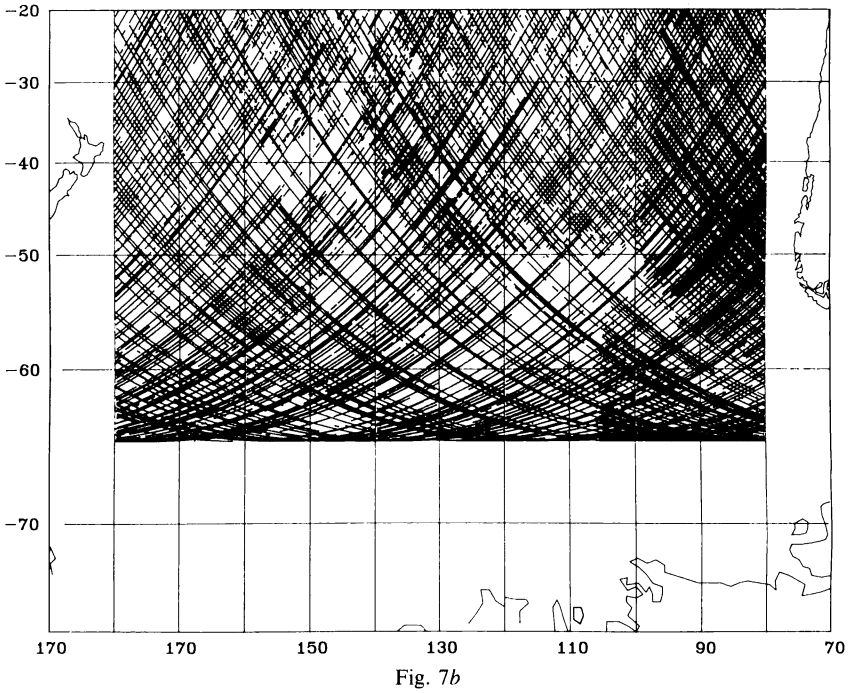

Fig. 7*b*

Fig. 7. Ground tracks of satellite altimeters. (*a*) SEASAT ground tacks are nearly uniform, except in sea ice areas (latitudes $< -65°$). Coverage is best at $-60°$. (*b*) GEOS 3 ground tracks are nonuniformly spaced. Best coverage occurs near tracking stations.

less uniform because the satellite could not store data between times of ground communication. Areas near tracking stations have higher data density than the more remote areas (Figure 7*b*).

To illustrate the quality of the SEASAT data, several examples of repeat passes over bathymetric features are shown in Figure 8. Three repeat profiles close to Easter Island are shown in Figure 8*a*. Each profile has a 2-m bump associated with the island, as well as smaller, less repeatable bumps to the north and south. The 1–2 m differences in bias among passes reflect the long-wavelength, radial errors in SEASAT'S ephemeris. Also shown (Figure 8*b*) are three repeat passes over the Eltanin FZ system. The large offset at about $-54°$ is associated with the age offsets across the Heezen and Tharp FZ's; the older seafloor lies to the north.

Low-pass filtered deflection of the vertical maps was produced from the network of passes shown in Figure 7. This was accomplished using the technique described in section 3. In practice, each of the four sets of parallel passes were differentiated and averaged into $0.1° \times 0.1°$ areas. Each set was then interpolated and filtered, using (18) with the weight function given in (20) and (21). Finally, the two components of the deflection of the vertical were estimated at every $0.1° \times 0.1°$ point by using (25), (8), and (9). The GEOS 3 data were weighted less heavily than the SEASAT data by making $\dot{\sigma}$ for GEOS 3 five times greater than $\dot{\sigma}$ for SEASAT (i.e., see (13)). In areas far from any SEASAT data and close to a GEOS 3 pass, however, the GEOS 3 data were more heavily weighted, since the weighting factor also depends upon the distance from a subsatellite track through (24). The results are insensitive to the relative SEASAT to GEOS 3 weights, except when the maps are based mostly on GEOS 3 data. In this case, the maps appear noisier.

Using the hill shading technique (section 3), enhanced images (Figures 9*a*, *b*) of the sun shining on the sea surface were constructed from the estimates of the deflections of the vertical. Since the deflection estimates were not high-pass filtered, at least two images are required to display the entire area. The region north of the Eltanin FZ and Louisville Ridge is most visible when the surface is illuminated from the NNE, as shown in Figure 9*a* (azimuth from east 80°). In this image, 50% gray corresponds to -1.50 μrad while the overall average range from black to white is 24 μrad (1 μrad = 0.206 arc sec). The southwest portion of the area appears best in Figure 9*b* where the illumination is from the SSW (azimuth 260°). The contrast level in this image is the same as Figure 9*a*; however, the 50% gray level was increased to 7.5 μrad. The brightest area in Figure 9*b* corresponds to the steep gradient in the geoid southeast of New Zealand. The random black and white variations south of $-65°$ are due to sea ice.

A partial failure of the interpolation technique is evident in the rippling along the Kermadec and Tonga trenches (upper left). This effect occurs because the geoid in this area is highly anisotropic and the weight function is narrower than the average spacing between parallel passes. The rippling can be reduced either by incorporating more data or by using an anisotropic interpolation technique. The latter remedy only hides the problem, however.

Tectonic Features

Besides the Tonga and Kermadec trenches, the most prominent tectonic features reflected in the geoid are the Eltanin FZ system, the Louisville Ridge, the Udintsev FZ, the Sala y Gomez Ridge, and the Nasca Ridge. The ocean rises do not appear strongly on the images because their spreading rates are relatively high and the geoid gradient is inversely proportional to spreading rate [*Sandwell and Schubert*, 1980]. The major fracture zones are displayed in more detail in Figure 10, where the illumination is from the south. The heavy white lines mark the axes of the East Pacific Rise and the Pacific Antarctic Ridge [*Weissel et al*, 1977]. The major FZ's, apparent on the bathymetric chart of the South Pacific [*Mammerickx et al.*, 1974], are shown as black lines. These locations agree fairly well with the FZ geoid signatures. The only disagreements occur at both ends of the Heezen FZ, where the black lines bend more sharply than the geoid signatures. The smaller FZ's lying to the north of the Eltanin FZ system are responsible for the rippled appearance of the geoid.

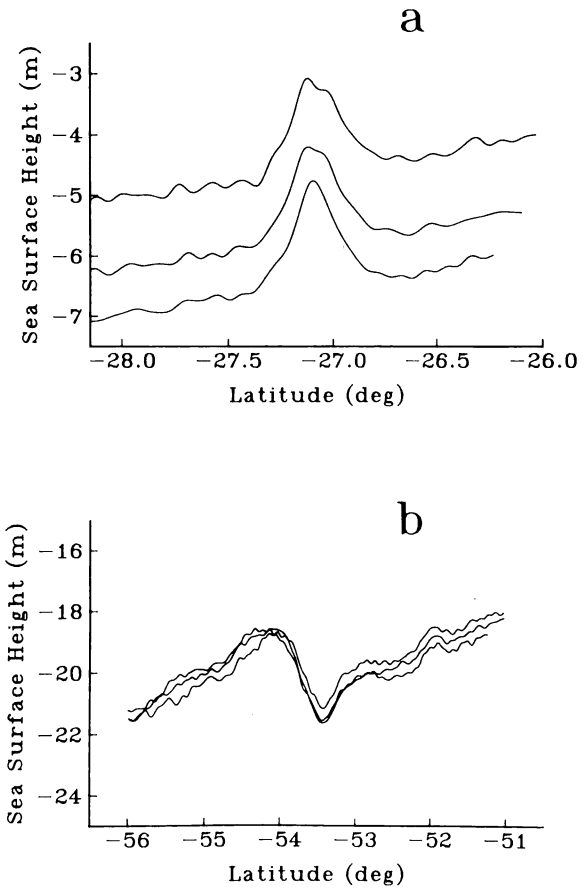

Fig. 8. SEASAT repeat passes over Easter Island (*a*) and the Eltanin FZ system (*b*). Large seamounts produce bumps on the sea surface, while fracture zones produce sharp steps. Amplitudes of the geoid undulations depend upon the amplitude of the topography and the mode of compensation.

Eltanin FZ and Louisville Ridge

The geoid signatures of the Eltanin FZ and the Louisville Ridge are connected at a longitude of 207° (Figure 9*b*). Together these two features extend more than 5000 km across the South Pacific. This connection was proposed by *Hayes and Ewing* [1968]. However, it could not be confirmed until now because bathymetric coverage of this area is very poor. At the connection point the geoid signatures of both tectonic features are small and they blend together. To the northwest the Louisville Ridge appears as a nearly continuous linear

bump in the geoid. The Eltanin FZ to the southeast has a steplike morphology.

Before discussing the braided signature of the Eltanin FZ system one must first understand the typical geoid expression of an isolated FZ. The Udinstev FZ, which is southeast of the Eltanin FZ system, has perhaps the clearest FZ geoid signal in the worlds's oceans. As discussed in section 1, geoid height decreases with increasing seafloor age; at an FZ it varies in a steplike manner because of the sharp age contrast. Across the Udintsev FZ, individual SEASAT profiles show smooth steps of 1–2 m. Looking northward, the step on the eastern section of the Udintsev FZ is positive (i.e., white in Figure 10), while it is negative (black) on along the western section. A small portion of the FZ lying at the midpoint of the two spreading ridges has zero age offset. At this point there is no depth offset and no geoid step. Thus plate tectonic theory, along with the geoid-age relation, explains the geoid signature of the Udintsev FZ.

This model also explains the more complex geoid signature of the Eltanin FZ system. The only difference is that the Eltanin system consists of two FZ's that are separated by only 50–70 km. As shown in Figure 10, the East Pacific Rise inter-

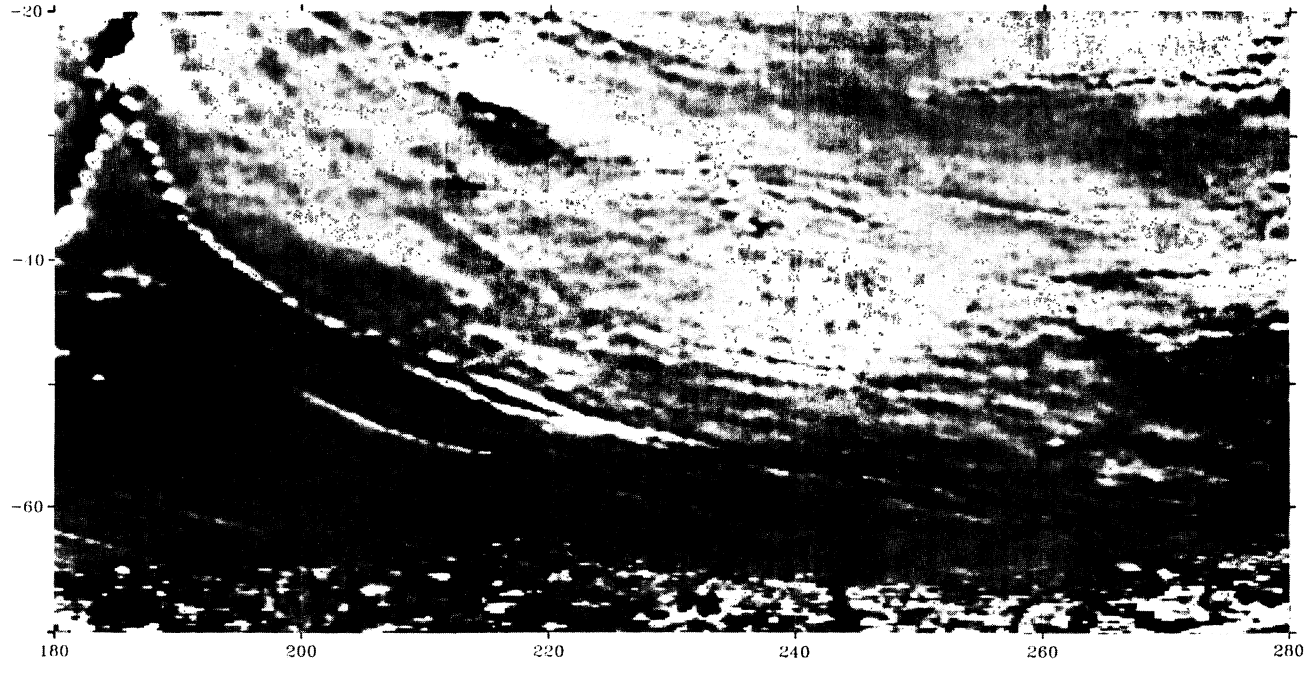

Fig. 9*a*

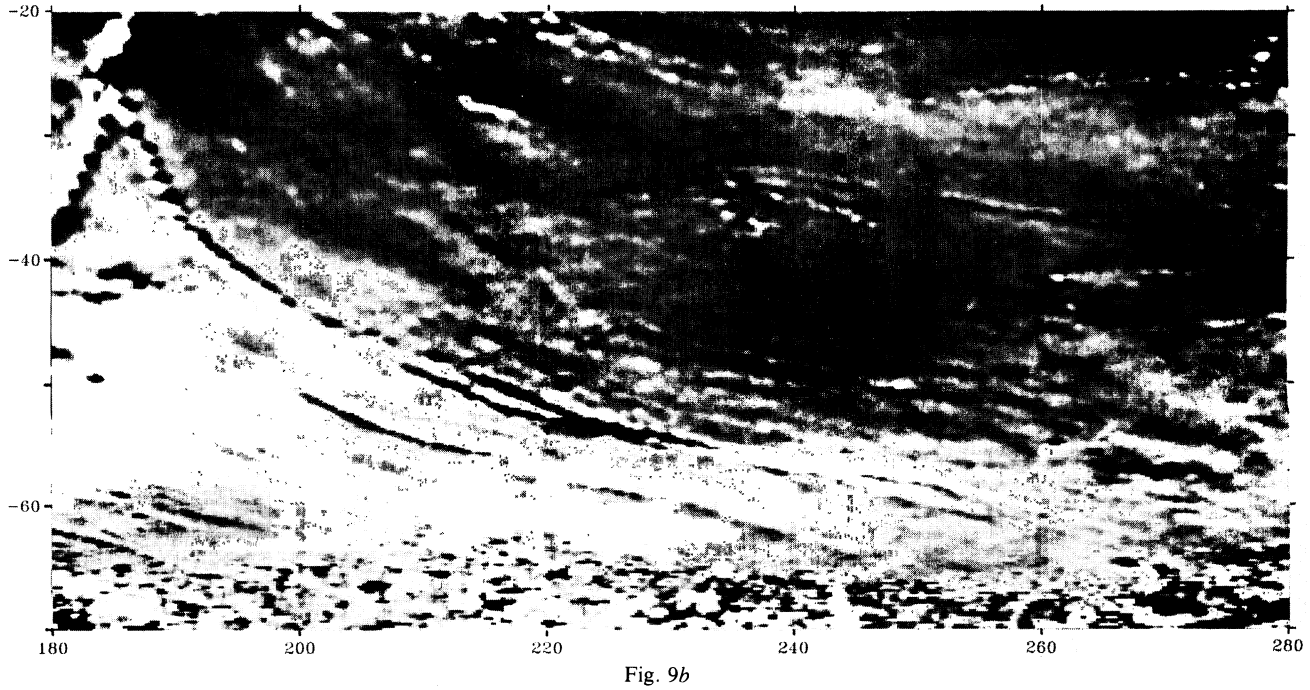

Fig. 9*b*

Fig. 9. Enhanced sun illumination images of the sea surface. (*a*) Illumination from the NNE (azimuth 80° from east) reveals many seamounts along the Sala y Gomez Ridge (upper right) as well as fracture zones crosscutting the East Pacific and the Chile rises. (*b*) Illumination from the SSW (azimuth 260°) reveals the Heezen, Tharp, and Udintsev FZ's. Smaller FZ's lie to the southwest. Also apparent are the Louisville Ridge and its connection with the Eltanin FZ system.

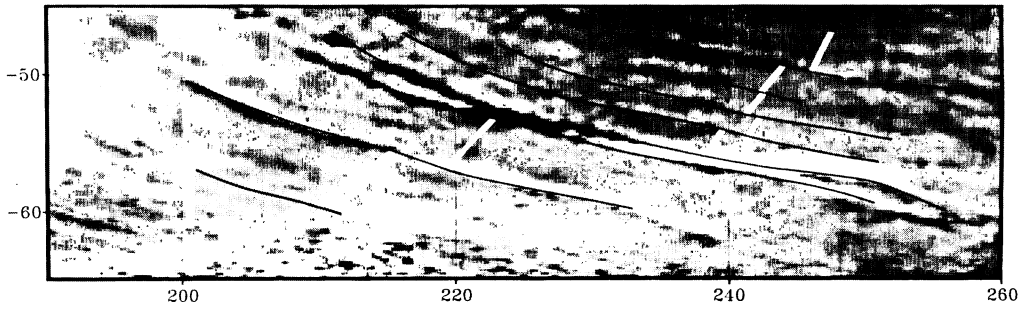

Fig. 10. Sun illumination image of the sea surface over major FZ's. Illumination is from the south. From north to south the major FZ's are the Heezen, the Tharp, and the Udinstev. Black lines mark known FZ's, while heavy white lines delineate spreading ridge axes.

sects the Tharp FZ at 222°, it is offset by both the Tharp and Heezen FZ's and emerges on the north side of the system at 239°. A short, uncharted segment of spreading ridge (not shown in Figure 10) lies between the two FZ's. Individually, the Heezen and Tharp FZ's produce geoid signatures that are similar to the geoid signature of the Udinstev FZ. The braided pattern results from the superposition of these two signatures. The divergences of the two signatures at the eastern and western ends of the Eltanin system reflect separations that are also apparent in the bathymetry. Where the spreading ridges intersect the system there are two geoid steps of the same polarity that are so close together they appear as a single step. At the midpoint between the two spreading ridges there is an upward step (white) across the Tharp FZ and a downward step (black) across the Heezen FZ. Since they are so close together at this point, the opposing signatures partially cancel one another. Gravity anomaly images produced from these data (W. F. Haxby, personal communications, 1983) show more pronounced braiding. Again this can be understood by considering the gravity signature of a single FZ, which is a ridge and trough rather than a step. Thus the gravity interference pattern produced by two FZ's in close proximity is quite complicated; it is also difficult to interpret in terms of the seafloor morphology. When examining the geoid, however, the braiding is less pronounced, and the signature of the Eltanin FZ system is easily understood as the superposition of two FZ geoid signatures in close proximity.

The origin of the Louisville Ridge is an unsolved problem of plate tectonic theory. There are two reasons for this. First, very little geophysical data has been collected in this remote ocean area. Indeed, the altimeter data presented here show that the ridge is more extensive than it appears on bathymetric charts. In addition, only a few seamounts along the northwest section of the Louisville Ridge have been dated, and the age of the surrounding seafloor is largely unknown because it was formed during the Cretaceous quiet period. Thus, it cannot be determined if the age progression of the seamounts is in accordance with the linear volcanic chain model.

The second reason that a formation model has not been established is that the Louisville Ridge does not have the morphology of other linear seamount chains, except possibly the Ninetyeast Ridge. For example, no other linear island chains are extensions of fracture zones. Also, most linear seamount chains consist of a series of individual seamounts; they are not as continuous or as narrow as the Louisville Ridge. *Larson and Chase* [1972] present convincing but inconclusive evidence that the Louisville Ridge overlays the older section of the Eltanin FZ. This hypothesis is in agreement with the geoid images (Figure 9*a*, *b*). A more recent study by *Watts and Ribe* [1984], using SEASAT data, demonstrates that the Louisville Ridge formed on mature lithosphere. They prefer a fractured plate model to explain the correspondence between geoid height and bathymetry.

Since hot-spot traces and FZ's are not necessarily parallel or coincident, it is highly unlikely that the Louisville Ridge was formed by the motion of the Pacific Plate over a nearly stationary hot spot. Instead, one must conclude that the FZ controlled the geometry of the Louisville Ridge. Furthermore, it is possible that the FZ itself somehow initiated volcanism. It should be noted that a similar situation occurred along the Ninetyeast Ridge, where a linear island chain overlays a large age-offset FZ [*Sclater and Fisher*, 1974]. This similarity is a strong indication that the Louisville Ridge and the Ninetyeast Ridge formed by similar mechanisms.

The hot-spot formation model is still viable, although the preexisting FZ must have guided the hot spot. There are a number of alternative models that should also be considered. (1) It is possible that whenever the age offset of a transform fault exceeds, say, 30 m.y., extreme thermal contrast along with shear heating could generate magma on the older plate. (2) *Turcotte* [1974] proposed that thermal contraction of the lithosphere is responsible for depressions along transform faults and fracture zones. If this model is correct then thermal contraction may create a void for magma leakage. (3) Another possibility is that the flexure caused by the difference in subsidence rates across an FZ [*Sandwell and Schubert*, 1982*b*] produces shear stresses that exceed the strength of the lithosphere, resulting in lithospheric failure followed by volcanism. Unfortunately, the available data do not discriminate among these possible models.

Seamount Locations

In addition to FZ's the images reveal many large seamount geoid signatures, especially Figure 9*a*. Seamounts can be distinguished from FZ's because (1) they are circular rather than linear, (2) they have both bright and dark sides, and (3) the bright side always faces the sun. Using these criteria, 210 seamount signatures were identified. To be unbiased, identifications were made without examining bathymetric charts. Each signature was assigned an intensity ranging from 1 (barely visible) to 5 (a major feature). The locations and sizes of these seamount signatures appear in Table 1. They are also plotted as X's in Figure 11*a*, where the size of each X is proportional to the intensity. To identify uncharted seamounts, the seamount locations in Table 1 were compared with the recent GEBCO map series [*Canadian Hydrographic*

TABLE 1. Location, Intensity, and Status of Seamount Geoid Signatures

Latitude	Longitude	Intensity*	Charted Uncharted
-27.55	185.63	5	C
-33.73	188.79	5	C
-35.44	189.68	5	C
-38.38	191.95	5	C
-40.49	194.52	5	C
-43.38	198.96	5	C
-27.65	215.80	5	C
-33.73	279.51	5	C
-65.00	267.01	5	C
-42.06	197.09	5	U
-45.39	202.57	5	U
-48.19	211.11	5	U
-54.85	261.19	5	U
-28.04	186.17	4	C
-30.20	186.62	4	C
-31.37	187.70	4	C
-39.85	193.93	4	C
-41.52	196.20	4	C
-42.06	187.21	4	C
-49.71	183.56	4	C
-26.81	213.53	4	C
-27.89	216.89	4	C
-21.96	221.09	4	C
-23.24	225.18	4	C
-35.05	234.12	4	C
-25.74	265.38	4	C
-26.18	280.00	4	C
-65.64	269.58	4	C
-45.98	205.68	4	U
-33.63	235.21	4	U
-36.08	234.91	4	U
-50.49	220.99	4	U
-41.23	261.23	4	U
-57.16	265.63	4	U
-32.45	188.25	3	C
-37.65	190.86	3	C
-39.12	193.09	3	C
-41.23	184.54	3	C
-41.37	186.22	3	C
-43.24	183.56	3	C
-47.79	180.30	3	C
-47.75	181.19	3	C
-22.11	202.27	3	C
-23.48	210.52	3	C
-24.41	211.31	3	C
-24.12	212.44	3	C
-21.72	219.65	3	C
-27.45	214.47	3	C
-20.39	220.74	3	C
-23.09	222.77	3	C
-34.85	232.25	3	C
-25.05	230.17	3	C
-26.03	259.46	3	C
-35.74	242.77	3	C
-25.10	261.04	3	C
-24.90	262.62	3	C
-25.59	266.91	3	C
-25.44	267.80	3	C
-25.39	268.74	3	C
-24.95	271.70	3	C
-25.78	276.84	3	C
-24.61	277.38	3	C
-23.43	278.07	3	C
-36.86	190.17	3	U
-42.60	197.97	3	U
-20.49	219.16	3	U
-28.82	218.42	3	U

Table 1. (Continued)

Latitude	Longitude	Intensity*	Charted Uncharted
-46.81	207.31	3	U
-29.02	239.16	3	U
-34.76	238.96	3	U
-37.11	227.90	3	U
-50.25	234.17	3	U
-51.81	227.01	3	U
-26.23	256.49	3	U
-36.37	245.09	3	U
-49.31	256.79	3	U
-22.06	278.91	3	U
-33.87	273.33	3	U
-45.98	260.89	3	U
-58.33	265.33	3	U
-57.35	268.49	3	U
-57.89	269.33	3	U
-29.07	180.40	2	C
-26.27	185.23	2	C
-42.21	188.74	2	C
-43.04	185.04	2	C
-21.42	200.64	2	C
-20.44	203.01	2	C
-21.96	205.43	2	C
-22.70	208.89	2	C
-25.29	211.65	2	C
-22.21	214.42	2	C
-21.91	215.65	2	C
-20.49	216.64	2	C
-49.02	219.75	2	C
-34.90	231.06	2	C
-47.25	224.00	2	C
-25.05	258.91	2	C
-27.06	250.57	2	C
-26.52	253.53	2	C
-26.47	254.86	2	C
-26.08	258.02	2	C
-35.15	241.53	2	C
-25.78	263.90	2	C
-25.64	270.47	2	C
-25.54	272.84	2	C
-25.88	275.70	2	C
-24.61	275.80	2	C
-20.88	279.26	2	C
-22.16	277.48	2	C
-36.91	188.99	2	U
-30.00	194.96	2	U
-30.69	195.70	2	U
-21.27	196.44	2	U
-23.04	197.92	2	U
-24.22	199.06	2	U
-26.03	199.26	2	U
-24.41	203.70	2	U
-30.93	209.48	2	U
-44.61	201.38	2	U
-46.18	204.30	2	U
-43.48	212.35	2	U
-42.16	213.18	2	U
-26.76	238.37	2	U
-31.86	222.57	2	U
-32.84	232.84	2	U
-32.50	233.93	2	U
-34.66	226.81	2	U
-35.20	228.25	2	U
-34.46	237.48	2	U
-36.57	233.23	2	U
-37.06	237.58	2	U
-51.67	223.46	2	U
-45.78	225.93	2	U

Table 1. (Continued)

Latitude	Longitude	Intensity*	Charted Uncharted
-25.10	259.75	2	U
-24.95	256.84	2	U
-27.30	256.15	2	U
-31.18	245.43	2	U
-35.78	243.75	2	U
-37.06	247.11	2	U
-37.45	245.23	2	U
-37.70	248.89	2	U
-39.22	257.92	2	U
-39.51	259.21	2	U
-39.90	247.11	2	U
-49.51	258.37	2	U
-43.63	262.47	2	U
-44.36	260.44	2	U
-44.66	261.78	2	U
-50.69	261.09	2	U
-57.40	272.84	2	U
-57.94	273.93	2	U
-60.59	272.34	2	U
-43.38	187.51	1	C
-23.28	209.38	1	C
-26.08	213.58	1	C
-26.67	215.06	1	C
-46.03	209.18	1	C
-47.89	213.83	1	C
-46.18	215.11	1	C
-34.46	231.65	1	C
-27.84	247.11	1	C
-27.16	257.28	1	C
-47.06	246.52	1	C
-25.10	260.15	1	C
-25.39	269.78	1	C
-26.76	270.96	1	C
-25.88	273.97	1	C
-24.66	274.57	1	C
-23.43	276.99	1	C
-23.68	205.78	1	U
-25.64	209.63	1	U
-26.23	210.91	1	U
-30.69	204.15	1	U
-36.76	219.36	1	U
-38.68	217.18	1	U
-38.82	218.72	1	U
-33.53	209.68	1	U
-33.12	211.65	1	U
-33.53	213.88	1	U
-39.02	206.07	1	U
-47.65	209.53	1	U
-41.42	211.46	1	U
-26.03	237.48	1	U
-35.29	224.84	1	U
-38.04	229.04	1	U
-39.31	225.73	1	U
-39.66	230.17	1	U
-39.61	231.26	1	U
-44.02	223.95	1	U
-46.62	221.78	1	U
-51.18	222.47	1	U
-22.89	240.40	1	U
-22.79	242.07	1	U
-21.32	248.64	1	U
-24.71	240.59	1	U
-26.91	241.19	1	U
-30.69	253.48	1	U
-25.49	253.53	1	U
-32.75	250.42	1	U

Table 1. (Continued)

Latitude	Longitude	Intensity*	Charted Uncharted
-37.06	246.32	1	U
-54.22	247.41	1	U
-28.82	261.04	1	U
-29.41	276.69	1	U
-29.41	277.48	1	U
-29.36	279.01	1	U
-29.36	279.75	1	U
-45.25	263.26	1	U
-46.57	262.07	1	U
-57.79	275.11	1	U

Location accuracies depend upon ground track spacing (e.g., ±50 km).

*Visual intensities range from 1 (barely visible) to 5 (major seamount).

Service, 1982]. The results of this comparison are as follows: (1) All large seamounts appearing on the bathymetric charts were identified on the geoid images, although locations differ by up to 50 km. (2) About half (112) of the seamount signatures identified on the geoid images were not charted. This is because, in all but a few cases, there are no bathymetry profiles lying within a radius of 50 km of the seamount geoid signature. (3) Seventy two of these uncharted seamounts have intensities greater than or equal to Easter Island's intensity (i.e., intensity of 2). (4) A group of more than 20 large seamount signatures lying between latitudes of $-40°$ and $-30°$ and longitudes of 225° and 245° were identified on the geoid images; only five of these seamounts were charted previously.

The locations of 72 suspected seamounts with intensities greater than 1 are plotted as O's in Figure 11*b*. They are also identified in Table 1. Whether or not seamounts actually exist at these locations depends upon how mass is distributed in the lithosphere; the relationship between geoid height and topography is nonunique. Many studies, however, demonstrate the high coherence between the gravity field and seafloor topography, especially at shorter wavelengths [*McKenzie and Bowin*, 1976; *Watts*, 1978; *McNutt*, 1979]. Based on these results, it appears that the seamounts identified in Table 1 exist and are located to an accuracy comparable to the spacing between altimeter passes (i.e., ~50 km). While it seems that uncharted seamounts can be located by this technique, it is impossible to estimate their sizes without a knowledge of the age of the lithosphere when the seamount formed [*Watts and Ribe*, 1984; also see Figure 2]. Therefore, there is no direct relationship between the size of the seamount and the intensity of its geoid signature. The intensity scale is used only to estimate the reliability of the prediction.

Seamount geoid signatures assigned intensities of 1 could possibly be false identifications, since they are barely visible on the geoid images. These identifications can be checked by examining individual altimeter passes over the suspected seamounts. A spot check was made in a relatively small area surrounding Easter Island. Four of the six intensity-1 seamounts in this area have geoid signatures of about 1 m on several altimeter passes. The existence of the other two seamounts is questionable, since one occurs along a fracture zone and the other appears only along GEOS-3 profiles.

A much higher degree of reliability can be placed on seamount signatures with intensities of 2 or more. For example,

Easter Island (intensity 2) produces an easily recognizable geoid signature on eight altimeter profiles; three of these are shown in Figure 8*a*. Two SEASAT profiles over an uncharted intensity-2 seamount are shown in Figure 12. By coincidence these two profiles have peak values at the point where they cross (−25.1°, 259.7°), and therefore they precisely mark the location of an uncharted seamount. The seamount signature to the south of the uncharted seamount reflects a charted seamount that is 3.2 km tall. Assuming the uncharted seamount formed concurrently with the charted seamount, its height is 2–3 km. Based upon the quality of the altimeter data and the generally good correspondence between geoid height and bathymetry, it is probable that a large seamount lies beneath every seamount geoid signature with intensity of 2 or more.

Hot-Spot Swells

The final type of geoid signature apparent in the geoid images (Figure 9*a*, *b*) are the longer-wavelength bulges associated with hot-spot swells. Hot-spot swell signatures are elongated in the direction of absolute plate motion and are 600 km or more wide. The most prominent swell signature in Figure 9*a* is centered at the Tubuai Islands (−25°, 215°). McDonald seamount, which is an active submarine volcano, lies at the southeast end of this swell. Like other hot-spot swells the ocean in this area is shallower than predicted by the depth-age

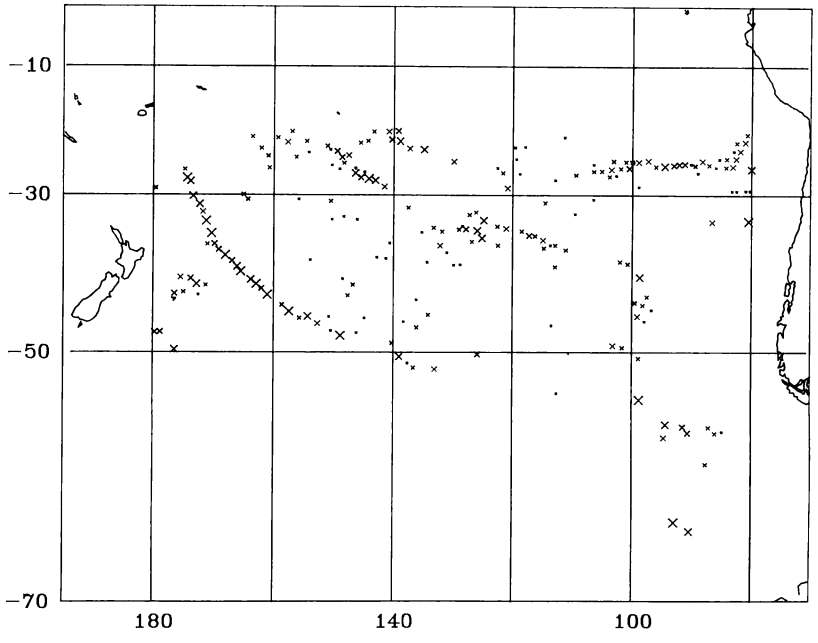

Fig. 11*a*

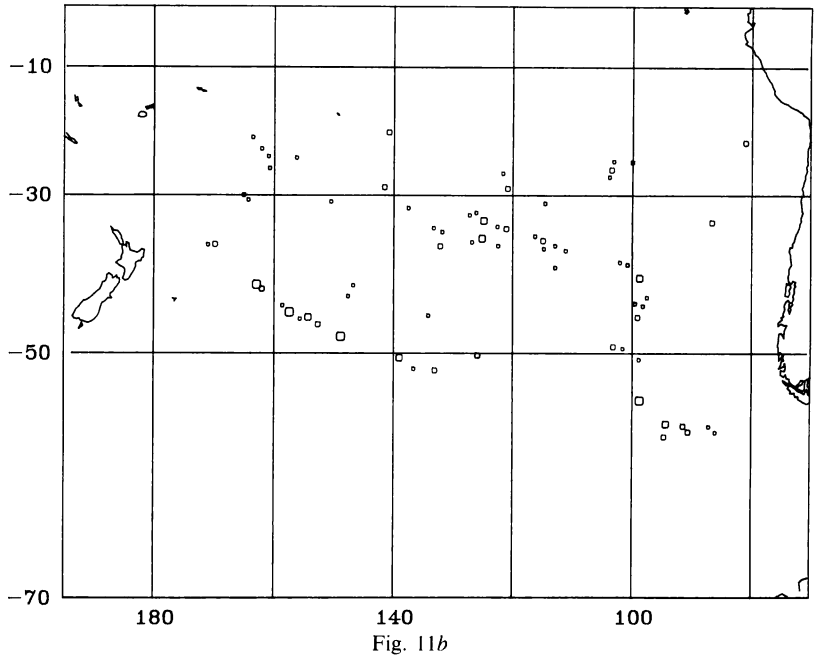

Fig. 11*b*

Fig. 11. (*a*) Locations of 210 seamount geoid signatures (X's). The size of X corresponds to the visual intensity of the circular geoid bump. (*b*) Locations of 72 seamount geoid signatures (O's with size proportional to visual intensity) that do not appear on bathymetric charts. Forty intensity-1 seamount geoid signatures are not shown.

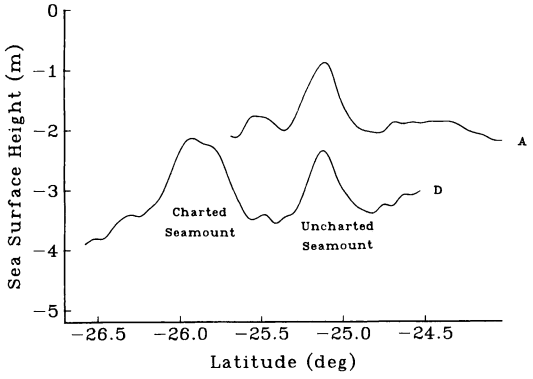

Fig. 12. Two SEASAT altimeter passes over an uncharted intensity-2 seamount located at −25.1°, 259.7° (A, ascending pass; D, descending pass). The other seamount geoid signature at −25.9° corresponds to a charted seamount lying only 330 m below sea level.

relation. A similar elongated geoid signature lies to the north of the Louisville Ridge and is centered at −40°, 205°. Bathymetric charts show a shoaling in this area; however, the coverage is extremely poor. *Dixon and Parke* [1983] have also noticed this feature in the geoid, although they attribute it to a large oceanic plateau.

Summary

1. Observations and theoretical models demonstrate that geoid height is highly correlated with seafloor topography for wavelengths less than 1000 km. This geoid/topography relationship is nonunique, however, because topography is compensated by a variety of mechanisms, including local compensation, regional compensation, and thermal compensation.

2. A technique was developed to construct images of shorter-wavelength geoid undulations from a dense network of SEASAT and GEOS 3 altimeter profiles. Data processing consists of along-track differentiation of each set of parallel profiles, interpolation between profiles, geoid gradient estimation, and image formation.

3. Analysis of SEASAT and GEOS 3 data over the South Pacific reveals many fracture zones and seamounts. Images show the detailed structure of the Eltanin and Udintsev FZ's, the connection between the Louisville Ridge and the Eltanin FZ, two hot-spot swells, and 72 previously undetected large seamounts.

Acknowledgments. I thank Russell Agreen for providing complete sets of GEOS 3 and SEASAT data, Carl Wagner for his helpful suggestions, and Tony Watts for his encouragement.

References

Banks, R. J., R. L. Parker, and S. P. Huestis, Isostatic compensation on a continental scale: Local versus regional mechanisms, *Geophys. J. R. Astron. Soc.*, *51*, 431–452, 1977.

Born, G. H., J. A. Dunne, and D. B. Lame, SEASAT mission overview, *Science*, *204*, 1405–1406, 1979.

Bracewell, R. N., *The Fourier Transform and Its Applications*, 444 pp., McGraw-Hill, New York, 1978.

Brammer, R. F., Estimation of ocean geoid near the Blake escarpment using GEOS 3 satellite altimetry data, *J. Geophys. Res.*, *84*, 3843–3851, 1979.

Brammer, R. F., and R. V. Sailor, Preliminary estimates of the resolution capability of the SEASAT radar altimeter, *Geophys. Res. Lett.*, *7*, 193–196, 1980.

Caldwell, J. G., and D. L. Turcotte, Dependence of the thickness of the elastic oceanic lithosphere on age, *J. Geophys. Res.*, *84*, 7572–7576, 1979.

Canadian Hydrographic Service, General bathymetric chart of the oceans (GEBCO), 5th ed., Ottawa, 1982.

Cazenave, A., B. Lago, and K. Dominh, Thermal parameters of the oceanic lithosphere estimated from geoid height data, *J. Geophys. Res.*, *88*, 1105–1118, 1983.

Crough, S. T., Thermal origin of mid-plate hot-spot swells, *Geophys. J. R. Astron. Soc.*, *55*, 451–469, 1978.

Crough, S. T., Geoid anomalies across fracture zones and the thickness of the lithosphere, *Earth Planet. Sci. Lett.*, *44*, 224–230, 1979.

Crough, S. T., and D. M. Jurdy, Subducted lithosphere, hot spots, and the geoid, *Earth Planet Sci. Lett.*, *48*, 15–22, 1980.

Den, N., et al., Seismic refraction measurements in the northwest Pacific Basin, *J. Geophys. Res.*, *74*, 1421–1434, 1969.

Detrick, R. S., An analysis of geoid anomalies across the Mendocino fracture zone: Implications for thermal models of the lithosphere, *J. Geophys. Res.*, *86*, 11,751–11,762, 1981.

Detrick, R. S., and S. T. Crough, Island subsidence, hot spots, and lithospheric thinning, *J. Geophys. Res.*, *83*, 1236–1244, 1978.

Detrick, R. S., and A. B. Watts, An analysis of isostasy in the world's oceans, 3, Aseismic ridges, *J. Geophys. Res.*, *84*, 3637–3653, 1979.

Dixon, T. H., and M. E. Parke, Bathymetry estimates in the southern oceans from SEASAT altimetry, *Nature*, *304*, 407–409, 1983.

Dorman, L. M. and B. T. R. Lewis, Experimental isostasy, 1, Theory of the determination of the earth's isostatic response to a concentrated load, *J. Geophys. Res.*, *75*, 3357–3365, 1970.

Douglas, B. C., R. E. Cheney, and R. W. Agreen, Eddy energy of the northwest Atlantic and Gulf of Mexico determined from GEOS 3 satellite altimetry, *J. Geophys. Res.*, *88*(C14), 9595–9603, 1983.

Griggs, D. T., The sinking lithosphere and the focal mechanisms of deep earthquakes, in *The Nature of the Solid Earth*, edited by E. C. Robertson, J. F. Hays, and L. Knopoff, pp. 361–384, McGraw-Hill, New York, 1972.

Gunn, R., A quantitative study of isobaric equilibrium and gravity anomalies in the Hawaiian Islands, *J. Franklin Inst.*, *236*, 373–390, 1943.

Hamilton, W. C., *Statistics in Physical Sciences*, 230 pp., The Ronald Press Company, New York, 1964.

Haxby, W. F., and D. L. Turcotte, On isostatic geoid anomalies, *J. Geophys. Res.*, *83*, 5473–5478, 1978.

Hayes, D. E., and M. Ewing, The Louisville ridge—A possible extension of the Eltanin fracture zone, in *Antarctic Oceanology 1*, edited by Joseph L. Reid, *Antarct. Res. Ser.*, vol. 15, pp. 223–228, AGU, Washington, D. C., 1968.

Horn, B. K. P., Hill shading and the reflectance map, *Geo-Processing*, *2*, 56–146, 1982.

Hussong, D. M., L. K. Wipperman, and L. W. Kroenke, The crustal structure of the Ontong Java and Manihiki oceanic plateaus, *J. Geophys. Res.*, *84*, 6003–6010, 1979.

Kaula, W. M., Global gravity and mantle convection, *Tectonophysics*, *13*, 341–359, 1972.

Kogan, M. G., Gravity field of oceanic block ridges, *Izv. Acad. Sci. USSR Phys. Solid Earth*, *12*, 710–717, 1976.

Lambeck, K., and R. Coleman, A search for seamounts in the southern Cook and Austral region, *Geophys. Res. Lett.*, *9*, 389–392, 1982.

Larson, R. L., and C. G. Chase, Late Mesozoic evolution of the Western Pacific Ocean, *Geol. Soc. Am. Bull.*, *83*, 3627–3644, 1972.

Lazarewicz, A. R., and D. C. Schwank, Detection of uncharted seamounts during satellite altimetry, *Geophys. Res. Lett.*, *9*, 385–388, 1982.

Lerch, F. J., R. P. Belott, E. M. Litkowski, and S. M. Klosko, Laser reference orbits and altimeter validation for GEOS 3, paper presented at Marine Geodesy Symposium, Rosenstiel School Mar. Atmos. Sci., Univ. Miami, Florida, 1978.

Lorell, J., M. E. Parke, and J. F. Scott, Geophysical Data Record (GDR) Users Handbook, 90 pp., report, Jet Propul. Lab., Pasadena, Calif., 1980.

Mammerickx, J., S. M. Smith, I. L. Taylor, and T. E. Chase, Bathymetry of the South Pacific, report, La Jolla Inst. Mar. Resour., Univ. Calif., San Diego, 1974.

Marsh, J. G., and T. V. Martin, The SEASAT altimeter mean sea surface model, *J. Geophys. Res.*, *87*, 3269–3280, 1982.

Marsh, J. G., and R. G. Williamson, Precision orbit analyses in support of the SEASAT altimeter experiment, *J. Astron. Sci.*, *28*, 345–369, 1980.

Marsh, J. G., T. V. Martin, J. J. McCarthy, and P. S. Chovitz, Mean sea surface computation using GEOS 3 altimeter data, *Mar. Geod.*, *3*, 359–387, 1980.

Mckenzie, D. P., and C. Bowin, The relationship between bathymetry and gravity in the Atlantic Ocean, *J. Geophys. Res.*, *81*, 1903–1915, 1976.

McNutt, M., Compensation of oceanic topography: An application of the response function technique to the *Surveyor* area, *J. Geophys. Res.*, *84*, 7589–7598, 1979.

Menard, H. W., and T. M. Atwater, Changes in direction of sea floor spreading, *Nature*, *219*, 463–467, 1968.

Rapp, R. H. GEOS 3 data processing for the recovery of geoid undulations and gravity anomalies, *J. Geophys. Res.*, *84*, 3784–3792, 1979.

Sailor, R. V., and E. A. Okal, Applications of SEASAT altimeter data in seismotectonic studies of the South-Central Pacific, *J. Geophys. Res.*, *88*, 1572–1580, 1983.

Sandwell, D. T., Thermal isostasy: Response of a moving lithosphere to a distributed heat source, *J. Geophys. Res.*, *87*, 1001–1014, 1982.

Sandwell, D. T., and K. A. Poehls, A compensation mechanism for the central Pacific, *J. Geophys. Res.*, *85*, 3751–3758, 1980.

Sandwell, D. T., and G. Schubert, Geoid height versus age for symmetric spreading ridges, *J. Geophys. Res.*, *85*, 7235–7241, 1980.

Sandwell, D. T., and G. Schubert, Geoid height-age relation from SEASAT altimeter profiles across the Mendocino fracture zone, *J. Geophys. Res.*, *87*, 3949–3958, 1982a.

Sandwell, D. T., and G. Schubert, Lithospheric flexure at fracture zones, *J. Geophys. Res.*, *87*, 4657–4667, 1982b.

Sclater, J. G., and R. L. Fisher, Evolution of the east central Indian Ocean, with emphasis on the tectonic setting of the Ninetyeast Ridge, *Geol. Soc. Am. Bull.*, *85*, 683–702, 1974.

Sibuet, J. G., and J. Mascle, Plate kinematic implications of Atlantic equatorial fracture zone trends, *J. Geophys. Res.*, *83*, 3401–3421, 1978.

Stanley, H. R., The GEOS 3 project, *J. Geophys. Res.*, *84*, 3779–3783, 1979.

Stanley, H. R., and R. E. Dwyer, NASA Wallops Flight Center GEOS 3 Altimeter Data Processing Report, 128 pp., NASA, Washington, D. C., 1980.

Turcotte, D. L., Are transform faults thermal contraction cracks?, *J. Geophys. Res.*, *79*, 2573–2577, 1974.

Walcott, R. I., Flexure of the lithosphere at Hawaii, *Tectonophysics*, *9*, 435–446, 1970.

Watts, A. B., An analysis of isostasy in the world's oceans, 1, Hawaiian-Emperor seamount chain, *J. Geophys. Res.*, *83*, 5989–6004, 1978.

Watts, A. B., and N. W. Ribe, On geoid heights and flexure of the lithosphere at seamounts, *J. Geophys. Res.*, in press, 1984.

Weissel, J. K., D. E. Hayes, and E. M. Herron, Plate tectonic synthesis: The displacements between Australia, New Zealand, and Antarctica since the late Cretaceous, *Mar. Geol.*, *35*, 231–277, 1977.

Wilson, J. T., Evidence from islands on the spreading of ocean flows, *Nature*, *197*, 536–538, 1963.

D. T. Sandwell, National Geodetic Survey, Charting and Geodetic Services, National Ocean Service, National Oceanic and Atmospheric Administration, Rockville, MD 20852.

(Received March 24, 1983;
revised October 11, 1983;
accepted October 12, 1983.)